Biomaterials 219 (2019) 119373

Contents lists available at ScienceDirect

Biomaterials

journal homepage: www.elsevier.com/locate/biomaterials

Bi-specific tenascin-C and fibronectin targeted peptide for solid tumor delivery

Prakash Lingasamy[a], Allan Tobi[a], Maarja Haugas[a], Hedi Hunt[a], Päärn Paiste[d], Toomas Asser[e], Tõnu Rätsep[e], Venkata Ramana Kotamraju[b,c], Rolf Bjerkvig[f], Tambet Teesalu[a,b,c,*]

[a] Laboratory of Cancer Biology, Institute of Biomedicine and Translational Medicine, University of Tartu, Tartu, 50411, Tartu, Estonia
[b] Cancer Research Center, Sanford Burnham Prebys Medical Discovery Institute, La Jolla, 92037, CA, USA
[c] Center for Nanomedicine and Department of Cell, Molecular and Developmental Biology, University of California, Santa Barbara, Santa Barbara, 93106, CA, USA
[d] Department of Geology, University of Tartu, 50411, Tartu, Estonia
[e] Department of Neurosurgery, Tartu University Hospital, 50406, Tartu, Estonia
[f] Department of Biomedicine Translational Cancer Research, University of Bergen, 5020, Bergen, Norway

ARTICLE INFO

Keywords:
Affinity targeting
Homing peptide
Extracellular matrix
GBM
Prostate carcinoma
Magnetic resonance imaging
Nanomedicine
T7 phage display

ABSTRACT

Oncofetal fibronectin (FN-EDB) and tenascin-C C domain (TNC-C) are nearly absent in extracellular matrix of normal adult tissues but upregulated in malignant tissues. Both FN-EDB and TNC-C are developed as targets of antibody-based therapies. Here we used peptide phage biopanning to identify a novel targeting peptide (PL1, sequence: PPRRGLIKLKTS) that interacts with both FN-EDB and TNC-C. Systemic PL1-functionalized model nanoscale payloads [iron oxide nanoworms (NWs) and metallic silver nanoparticles] homed to glioblastoma (GBM) and prostate carcinoma xenografts, and to non-malignant angiogenic neovessels induced by VEGF-overexpression. Antibody blockage experiments demonstrated that PL1 tumor homing involved interactions with both receptor proteins. Treatment of GBM mice with PL1-targeted model therapeutic nanocarrier (NWs loaded with a proapoptotic peptide) resulted in reduced tumor growth and increased survival, whereas treatment with untargeted particles had no effect. PL1 peptide may have applications as an affinity ligand for delivery of diagnostic and therapeutic compounds to microenvironment of solid tumors.

1. Introduction

Targeting of anticancer drugs with affinity ligands, such as antibodies and homing peptides, is widely used to achieve a balance between increased drug concentration at the tumor site and reduced systemic exposure [1,2]. In particular, antibody drug conjugates (ADCs) have seen clinical successes with 4 ADCs clinically approved and > 100 in different stages of clinical testing [3]. However, antibodies are expensive to manufacture and show poor tissue penetration due to a combination of large size and high affinity [4]. *In vivo* peptide phage display, an agnostic explorative technique, has been used to probe vascular heterogeneity of live animals and to identify tumor homing peptides [5]. As phage used for *in vivo* display is a nanoparticle itself, the peptides are particularly well-suited for delivery of nanoparticle payloads [2]. Homing peptide target molecules (receptors) include different cell surface molecules: e.g., αv-integrins, NRP-1, folate receptor alpha, Ephrin receptor A2 (EphA2), molecules aberrantly expressed on the surface of tumor and stromal cells (e.g. p32, nucleolin, and calreticulin), components of blood clots, and the tumor extracellular matrix (ECM) [6–12].

Certain ECM proteins (e.g., periostin, hyaluronan, certain collagens, laminins, perlecan, fibronectin, and tenascins) are over-represented in the tumor microenvironment and may provide a more stable and high capacity target for affinity delivery than antigens expressed on the cell surface [13]. Alternatively spliced fibronectin Extra Domain-B (FN-EDB) and Tenascin-C (TNC) are overexpressed in many solid tumors [14–16]. TNC isoform C (TNC-C) shows particularly low baseline expression in non-malignant tissues and a robust upregulation in solid tumors such as malignant brain tumors and lung carcinoma [14,15]. The FN-EDB and TNC antibodies (FN-EDB ScFV L19, TNC-C ScFV G11, F16, and 81C6) are used for precision delivery of cytokines (e.g., IL2, TNF) and radionuclides [17,18]. In addition, these antibodies are evaluated as diagnostic imaging agents for immuno-PET, SPECT/CT and radioimmunotherapy in malignant primary and metastatic brain tumors, and in head- and neck squamous cell carcinomas [17–19]. Importantly, recent studies demonstrate that ECM-directed non-

* Corresponding author. Laboratory of Cancer Biology, Institute of Biomedicine and Translational Medicine, University of Tartu, Tartu, 50411, Tartu, Estonia.
E-mail address: tambet.teesalu@ut.ee (T. Teesalu).

https://doi.org/10.1016/j.biomaterials.2019.119373
Received 2 April 2019; Received in revised form 8 July 2019; Accepted 18 July 2019
Available online 19 July 2019

internalizing antibodies can be used to potentiate the cytotoxic activity of intracellularly acting cytotoxic drugs [20].

Simultaneous affinity targeting of multiple molecules in the tumor-associated ECM is advantageous over targeting one receptor at the time. First, expression of the tumor ECM is heterogeneous and multitargeting may result in a more uniform biodistribution of payloads. Secondly, dual targeting may alleviate issues related to limited number of available receptors for affinity ligands - a major bottleneck in affinity targeting [21].

Here we identified a novel bispecific peptide (PL1; amino acid sequence: PPRRGLIKLKTS) that recognizes both FN-EDB and TNC-C and show that this dual-targeted peptide can be used for robust and specific delivery of imaging agents and therapeutic payloads to solid tumors.

2. Materials and Methods

2.1. Materials

Phosphate-buffered saline (PBS) was purchased from Lonza (Verviers, Belgium), $K_3[Fe(CN)_6]$, HCl, Nuclear Fast Red, Xylene substitute, isopropanol, Triton-X, Tween-20, $CHCl_3$, MeOH, and dimethylformamide (DMF) were purchased from Sigma-Aldrich (Munich, Germany). Cloning, expression, purification of proteins (FN-EDB, TNC-C, NRP1, NCL and single chain antibodies FN-EDB-L19 and TNC-C-G11), and generation of polyclonal rabbit antibodies are described in Supplementary Information, Materials and Methods section.

2.2. Cell lines

U87MG and PC3 prostate carcinoma cells were obtained from ATCC, and NCH421K cells from CLS Cell Lines Service GmbH (Eppelheim, Germany). WT-GBM and VEGF-KO GBM cells were a kind gift from Gabriele Bergers (Leuven, Belgium).

2.3. Clinical samples

Fresh surgical samples of GBMs were obtained from Tartu University Clinics, Tartu, Estonia under protocols approved by the Ethics Committee of the University of Tartu, Estonia (permit #243/T27).

2.4. Animal experiments

Animal experimentation procedures were approved by the Estonian Ministry of Agriculture, Committee of Animal Experimentation, project #42 and #48. Athymic nude mice (HD) were housed in a pathogen-free environment at the Animal Facility of the Institute of Biomedicine and Translational Medicine, University of Tartu (Tartu, Estonia). For tumor modeling, we used nude mice bearing orthotopic GBM (NCH421K, U87MG and, WT-GBM) and s.c. prostate carcinoma (PC3). For orthotopic GBM induction, the mice were placed into the ear bars of a stereotactic frame, a midline incision was made using a scalpel exposing the sagittal and coronal sutures, and a burr hole was scraped through the skull 0.5 mm anterior to the bregma and 2.5 mm lateral to the midline using a syringe. GBM 300,000 cells in 3 μL PBS were injected at a depth of 3 mm with a Hamilton syringe over 4 min, and the needle was removed 5 min after the injection. Bone wax was used to close the burr hole, the surface was cleaned with a sterile cotton swab, and the skin was closed by sutures.

2.5. Phage biopanning

We used for biopanning the NNK-encoded cyclic CX7C, and linear X7 peptide libraries (diversity $\sim 5 \times 10^8$) displayed on T7 415-1b phage scaffold (Novagen, EMD Biosciences, MA, USA). To identify bispecific peptides that interact with both TNC-C and FN-EDB, we performed cross screens on both targets. During the first round of selection, microtiter plates coated with 20 μg/ml recombinant purified TNC-C were blocked with PBS containing 1% bovine serum albumin (BSA), followed by incubation with 5×10^8 pfu of phages in PBS at 4 °C overnight, by washes to remove background, and by phage rescue and amplification in BLT5403 strain of *E. coli* (Novagen, EMD Biosciences, MA, USA) [5]. The following rounds of biopanning were carried on Ni-NTA Magnetic Agarose Beads (QIAGEN, Hilden, Germany) coated with hexahistidine-tagged FN-EDB (3 μg/μl beads) at room temperature. After 5 rounds of selection, a set of random clones was sequenced, and individual peptide-phage clones and control (G7 peptide-displaying or insertless) phages were incubated with FN-EDB and TNC-C-coated magnetic beads. RPARPAR phage and His-tagged NRP-1 b1b2 domain were used as positive control [22]. To address the specificity of the peptide phage binding to the FN-EDB and TNC-C, the protein-coated beads were pre-incubated with 20 μg/ml blocking rabbit polyclonal antibodies.

2.6. Synthesis of peptides and nanoparticles

The peptides were synthesized in-house or ordered from TAG Copenhagen (Frederiksberg, Denmark). Peptides were synthesized using Fmoc/*t*-Bu chemistry on the microwave-assisted automated peptide synthesizer (Liberty, CEM Corporation, NC, USA), purified by HPLC using 0.1% TFA in acetonitrile-water to 90%–95% purity, and validated by Q-TOF mass spectral analysis. All peptides were synthesized with free carboxyl termini; 5(6)-carboxyfluorescein (FAM) or biotin was attached via the 6-aminohexanoic acid spacer to the N-terminus of the peptide. The iron oxide nanoworms (NWs) were prepared according to a published protocol by Ref. [23] with minor modifications. The aminated NWs were PEGylated using maleimide-5K-PEG-NHS. Peptides were coupled to NWs through a thioether bond between the thiol group of a cysteine residue added to the N-terminus of the peptide and the maleimide on the functionalized particles. Isotopically pure silver nanoparticles (AgNPs) were synthesized and functionalized as previously described [6]. For more details on nanoparticle preparation and characterization, see Supplementary Information, Materials and Methods section.

2.7. Cell-free peptide-binding assay

The FAM-labeled peptides were coated on ELISA plates (Nunc Maxisorp, Thermo Fisher Scientific Inc., MA, USA), blocked with PBS containing 1% BSA, and incubated with recombinant proteins at 2μg/well in PBS for 6 h. The protein was detected using an anti-His-tag antibody, followed by horseradish peroxidase-conjugated secondary antibody, chromogenic reaction, and measurement of absorbance at 450 nm with a microplate reader (Tecan Austria GmbH, Grödig, Austria).

2.8. Laser ablation ICP-MS-based AgNP biodistribution studies

Isotopically pure Ag^{107}NPs and Ag^{109}NPs were prepared as described [6] and functionalized with biotinylated PL1 peptide (PL1-Ag^{109}NPs) or biotin (biotin-Ag^{107}NPs) particles. PL1-functionalized and control AgNPs were mixed at 1:1 ratio and injected i.v. in nude mice bearing U87MG orthotropic GBM. 5 h later, the mice were perfused via the left ventricle of the heart with 20 mL PBS. Organs were snap-frozen for cryosectioning and ICP-MS analysis. Snap-frozen organs were cryosectioned (30 μm) and stored at −20 °C. Before the LA-ICP-MS analysis, the samples were thawed and dried in a desiccator.

Mapping of ^{109}Ag and ^{107}Ag isotopes on tissue sections (2-D mapping and line scans) was performed using a Cetac LSX-213 G2+ laser ablation (LA) system using a HelEx 2-volume ablation cell, coupled to Agilent 8800 QQQ ICP-MS. The LA-ICP-MS setup was optimized using NIST 612 glass. Main parameters for LA–ICP–MS are shown in Table S1.

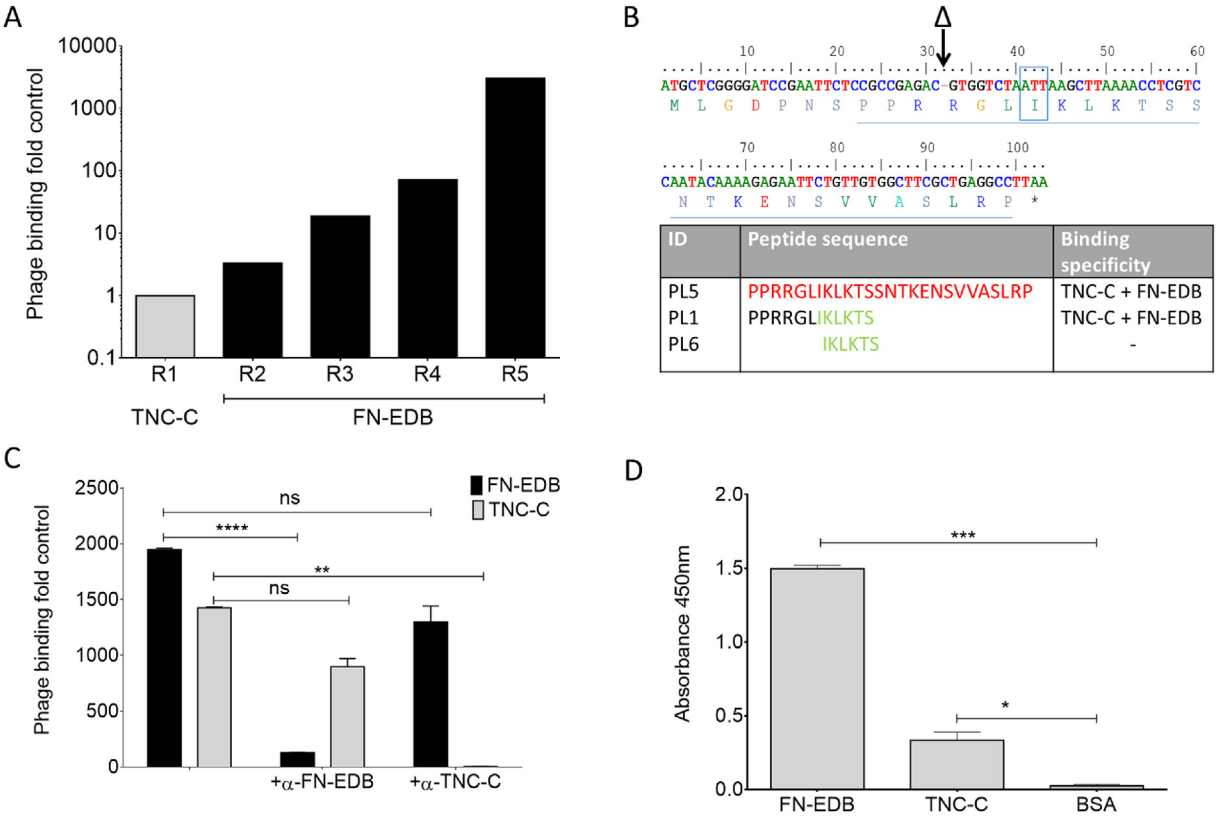

Fig. 1. Identification of bispecific peptide targeting FN-EDB and TNC-C. (A) Biopanning using T7 phage-displayed X7 peptide library on immobilized TNC-C and FN-EDB resulted in ~3000-fold enrichment in binding to FN-EDB in round 5 of selection. (B) Genomic DNA and amino acid sequence of the C-terminal portion of the T7 major coat protein 10 and the adjacent exogenous PL5 peptide (underlined); single nucleotide deletion in the peptide-encoding DNA is indicated by an arrow. PL5 and its shorter derivative PL1 peptide retain the ability to bind both target proteins. (C) PL1 phage binds to immobilized FN-EDB and TNC-C. The specificity of PL1-phage binding to EDB and TNC-C was evaluated by preincubation of protein-beads with 50 μg/ml of anti-FN-EDB or anti-TNC-C blocking antibody. PL1 phage binding is expressed as fold over control phage displaying heptaglycine. (D) Synthetic PL1 peptide interacts with FN-EDB and TNC-C proteins. Immobilized FAM-PL1 was probed with recombinant His-tagged EDB and TNC-C (or control BSA), followed by sequential incubation with rabbit anti–His-tag primary antibody, secondary goat anti-rabbit HRP antibody and a chromogenic peroxidase reaction. Values represent mean ± standard deviation from 3 independent experiments; P-values were determined by Student unpaired t-test; all statistical tests were two-sided; *P < 0.05; **p < 0.01; ****p < 0.0001.

^{13}C, ^{107}Ag, and ^{109}Ag isotopes were detected with dwell times of 9.5 and 14 ms respectively, corresponding to a duty cycle of 0.05 s ^{13}C was used as an internal standard to account for differences in the volume of ablated tissue. Data reduction and elemental and isotope ratio maps were constructed using Chromium 2.2 and Iolite v3.62 software.

Multiple parallel line raster scans were performed to generate distribution maps. The raster lines were directly adjacent to each other (with 65 μm offset) and the whole mapping area was ablated. A typical sample area was ~14 × 8 mm, and run time for a single sample was ~4 h.

2.9. In vivo NW biodistribution studies

NWs (7.5 mg/kg) in PBS were injected into the tail vein of the tumor-bearing mice, followed by cardiac perfusion with 20 ml PBS/DMEM before collection tumor and control organs for imaging. In control experiments, NW injection was preceded by systemic pre-injection of blocking FN-EDB and/or TNC-C antibodies (30 μg/mouse) 15 min prior to injection of the NWs.

2.10. Confocal microscopy

Snap-frozen 10 μm tumor cryosections were mounted on Superfrost™+ slides. The sections were equilibrated at RT and fixed with 4% paraformaldehyde or methanol and permeabilized with PBST (PBS + 0.05% Tween 20), blocked with PBST, 5% BSA, 5% goat serum (GE Healthcare, Little Chalfont, UK) at RT for 30 min, followed by primary antibody incubation at RT for 1 h. The primary antibodies were rabbit anti-fluorescein IgG (cat. no. A889, Thermo Fisher Scientific, MA, USA), rat anti-mouse CD31 (BD Biosciences, CA, USA), mouse anti-human nestin (#MA1-110, Thermo Fisher Scientific Inc.), rat anti-mouse CD31, rat anti-mouse CD11b (cat. no. 553370; 557395, BD Biosciences, CA, USA), rat anti-mouse LYVE-1 (cat. no. 14044382, eBioscience, CA, USA), rat anti-mouse CD68 (#MCA1957A488, Bio-Rad, CA, USA), rabbit polyclonal anti-Ki67 (cat. no. NB500-170, Novusbio, UK), and rabbit anti-cleaved caspase-3 (cat. no. 966, Cell Signaling Technology, MA, USA), and in-house prepared CF647 (or CF546)-labeled single chain antibodies ScFV L19 (against FN-EDB) and ScFV G11 (against TNC-C). The secondary antibodies, Alexa 488 goat anti-rabbit IgG, Alexa 647 goat anti-rat IgG, and Alexa 546 goat anti-mouse IgG, were from Invitrogen (USA). Nuclei were counterstained with DAPI (Molecular Probes) at 1 μg/ml. The coverslips were mounted on glass slides with Fluoromount-G (Electron Microscopy Sciences, PA, USA), imaged using confocal microscopy (Olympus FV1200MPE, Tokyo, Japan) and analyzed using the FV10-ASW4.2 viewer, Imaris software and ImageJ freeware.

2.11. NW overlay assay

Fresh surgical GBMs (obtained during autopsy) were snap-frozen in liquid nitrogen, cryosectioned at 8 μm, fixed with methanol, and permeabilized with TBS followed by blocking buffer containing 5% BSA,

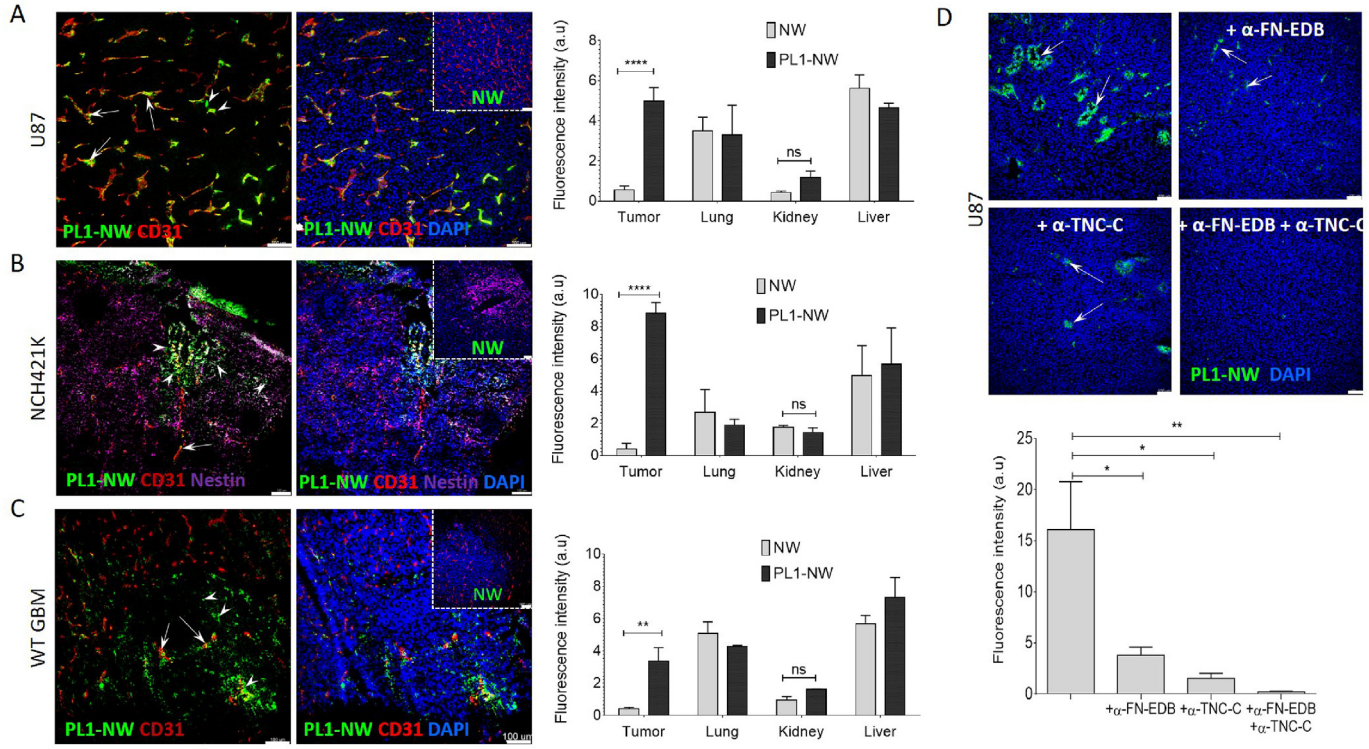

Fig. 2. Systemic PL1-NWs home to glioblastoma lesions. (A, B, C) NWs coated with FAM-labeled PL1 peptide or control FAM-NWs were i.v. injected at 7.5 mg/kg into mice bearing s.c. U87MG (A), orthotopic NCH421K (B), and orthotopic WT GBM (C) glioblastoma xenografts. After 5 h circulation, the mice were perfused through the heart with PBS/DMEM and organs were collected. Cryosections were immunostained with antibodies against fluorescein to visualize NWs (green), endothelial cells (CD31, red), and stem cell-like cells (nestin in NCH421K, magenta) and examined using confocal microscopy. Images acquired under same conditions from tumor sections from mice injected with control non-targeted FAM-NWs are shown in the boxes). The arrows point to PL1-NWs (green) along the tumor blood vessels and the arrowheads point to extravasated PL1-NWs. FAM signal was quantitated by Fiji ImageJ (A-C, bar charts on the right). (D) Specificity of in vivo homing of PL1 nanoparticles probed with antibody blockade. PL1-NWs (7.5 mg iron/kg body weight) alone, or in combination with individual anti-EDB, or anti-TNC-C antibodies, or a cocktail of both antibodies, were i.v. injected into mice bearing U87 xenograft tumors. Five hours after the injection, the mice were perfused through the heart with PBS/DMEM and organs were collected for cryosectioning and examination by confocal microscopy. Arrows point to PL1-NWs (green) in tumor tissue. Nuclei were stained with DAPI (blue). The FAM signal was quantified from representative images using Fiji ImageJ. Error bars, mean ± SEM (N = 3–6 mice per group); scale bars: 100 μm; p-value was determined using Student unpaired t-test, two-tailed; ns $P > 0.05$; *$P < 0.05$; **$p < 0.01$; ****$p < 0.0001$.

5% goat serum and 5% FBS in TBS. For overlay, the sections were incubated with 20 μg/slide of PL1-NW or NW at 4 °C overnight. The sections were washed and blocked with blocking buffer, followed by immunostaining using rabbit anti-fluorescein primary antibodies and detection with the Alexa-488 anti-rabbit secondary antibody. FN-EDB and TNC-C were detected by fluorescently labeled single-chain antibodies ScFV L19 FN-EDB-CF647 and ScFV G11 TNC-C-CF555.

2.12. In vivo angiogenesis model and multiphoton intravital imaging

Angiogenesis was induced by injecting 2.5×10^8 PFU of an adenoviral vector driving expression of mouse $VEGF^{164}$ ($Ad\text{-}VEGF^{164}$) intradermally into the left ear of 7–8 week-old female nude mice [24]. The right ear served as a control. PL1-NW or NW (at 7.5 mg/kg) were i.v. injected 4 days after induction of angiogenesis and 24 h before intravital imaging. Texas Red/Evans Blue was i.v. injected at 30 mg/kg to allow visualization of blood vessels. The ear was fixed on the coverslip for imaging using a veterinary-grade glue tape, and a mold was prepared around the ear from agarose for imaging. The body temperature was maintained throughout the experiment with a heat mat. Images and videos were acquired at an excitation wavelength of 920 nm, optical sections were taken under identical conditions, and experiments were repeated in triplicates. Intravital imaging was performed with multi-photon laser scanning fluorescence microscope (Olympus FV1200MPE-BX61WI) equipped with MaiTai DeepSee IR laser (Spectra-Physics) and with XLPLN25x/1.05 NA water-immersion objective (Olympus).

2.13. Magnetic resonance imaging

For MRI, nude mice bearing orthotopic NCH421k GBM were i.v. injected with iron oxide nanoworms at 5 mg/kg. Five hours after NW injection, the mice were anesthetized with isoflurane and subjected to MRI using a 9.4 T BioSpec 94/21 (Bruker BioSpin MRI GmbH, Ettlingen, Germany) equipped with ParaVision Acquisition 6.0.1 software (Bruker, Ettlingen, Germany). Following intravital MRI, the animals were perfused with PBS to remove blood and background circulating NWs and subjected to postmortem MRI. After imaging, tumors and control tissues were harvested and sectioned for immunofluorescence staining. Mice received isoflurane in oxygen mix (1.5%, flow rate of 200 ml/min) for anesthesia; the body temperature and breathing rate were monitored throughout the experiments. T2* map MGE (Multiple Gradient Echo) sequences were acquired in sagittal and coronal orientations. The following parameters used during the data acquisition were the following: slice thickness, 0.375 mm (3 slices averaged offline for improved signal/noise ratio); inter-slice gap: 0.375 mm; repetition time: 800; Echo time: 3.5–38.5 ms; flip angle: 50°; number of axial slices: 128; pixel bandwidth: 292.9; imaging frequency: 400.3; matrix: 256 × 256; magnetic field strength: 9.4. To calculate T2 relaxation times, regions of interest (ROIs) were drawn manually on the images by using image sequence analysis (ISA) tool package (Paravision 5, Bruker) using T2vtr fit function y = A + C*exp (-t/T2) (A: absolute

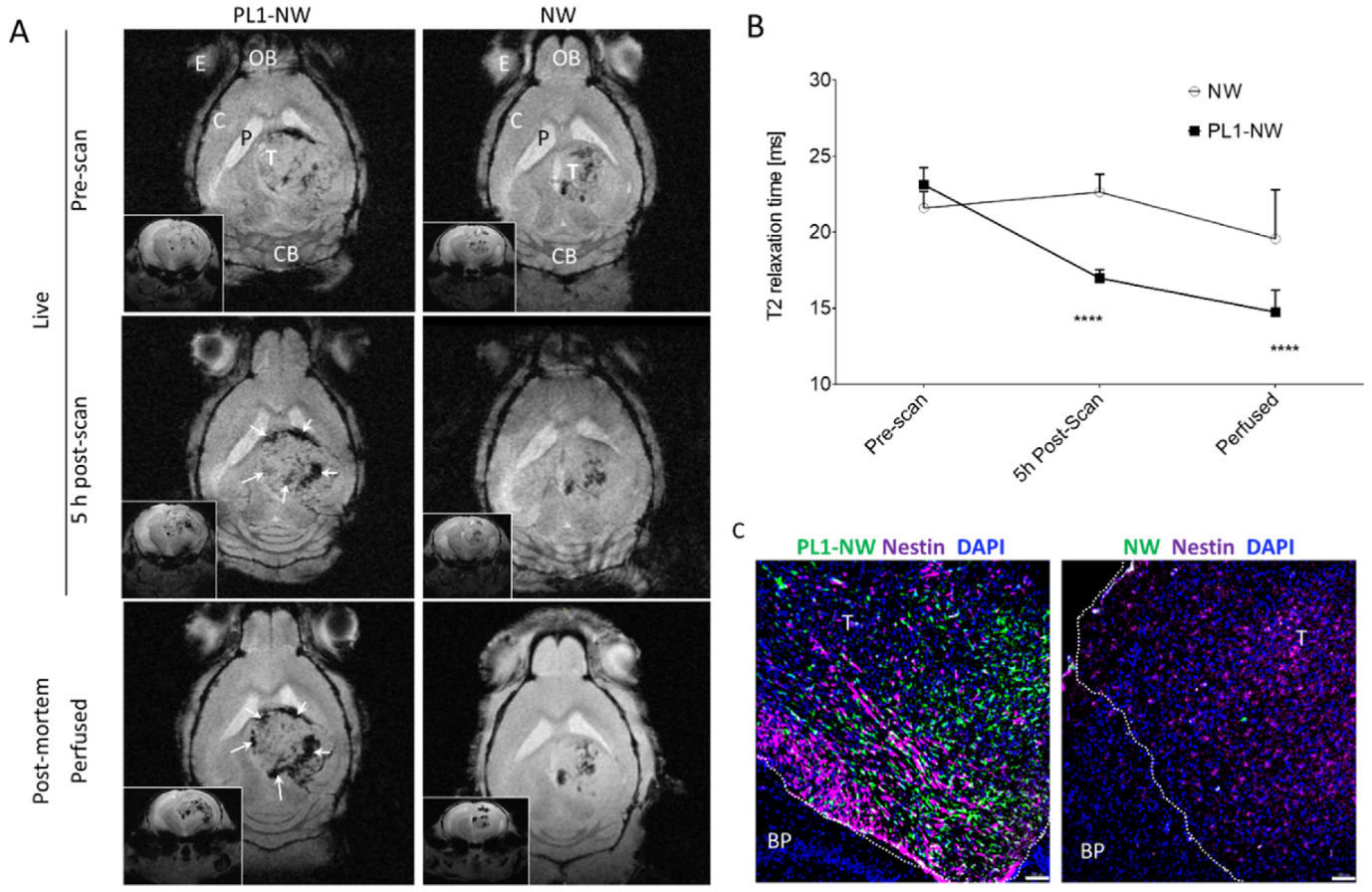

Fig. 3. T2-weighted and T2* MRI of orthotopic NCH421K glioma mice. NCH421K glioblastoma mice were i.v. injected with PL1-NWs or control NWs (5 mg/kg iron). (A) Axial slice views of T2-weighted images prior to NW injection (pre-scan), at 5 h after NW circulation (post-scan), and terminal images after perfusion with PBS to remove blood and circulating NWs (perfused; T, tumor). Note increased dark signal in a tumor of a mouse injected with PL1-NWs (arrows), but not with control NWs. Insets: coronal T2-weighted views of same tumor. Representative images from 3 independent experiments are shown. (B) T2 parametric image (T2* map) used for T2-relaxation time plot, showing targeted and non-targeted NW relaxation time in ms. P-value was determined by one-way ANOVA with Dunnett's multiple comparisons test in comparison with pre-scan; *P $<$ 0.05; ***P $<$ 0.001; ****p $<$ 0.0001, error bars: mean $\pm$ SEM, (3 mice per group, for each time point 10–11 data points/mouse). (C) Confocal imaging of cryosections from mice used for MRI studies. Green: NWs, magenta: anti-human nestin; blue: nuclei stained with DAPI; White arrows point to localization of PL1-NWs in the tumor (T) defined by the presence of high nuclear density; BP - normal brain parenchyma. The dotted line shows the tumor margin. Scale bars, 100 µm.

bias; C: signal intensity; T2: spin-spin relaxation time) for T2 evaluation. To calculate mean signal intensity in the tumor to a reference region, ROIs were drawn manually on the images at given echo time (TE). Experiments were repeated in triplicate.

2.14. Experimental tumor therapy

U87MG cells (4×10^6 cells) in 100 µl PBS were implanted subcutaneously into the right flank of 11–15 week old male nude mice. The weight of animals and tumor volume [length $\times$ (width x width)/2] was recorded on every other day until tumor volume reached ~100 mm^3. Animals were randomized into 4 groups (PBS, FAM-$_D$[KLAKLAK]$_2$-NWs, FAM-PL1-NWs, and FAM-PL1-$_D$[KLAKLAK]$_2$-NWs; 8 mice/group). 100 µl of NWs (at 5 mg/kg body weight of iron) or PBS was intravenously injected into the tail vein every other day for ten injections. Tumor size, body weight, survival, and behavior were recorded during treatment and post-therapy. When the tumor volume reached 2000 mm^3 (or > 10% body weight), the mice were sacrificed, and organs and tumors were excised, macroscopically observed and snap frozen. Tumor volume, Kaplan–Meier survival and body weight curves were calculated using the GraphPad Prism 6 software with p-values < 0.05 considered significant. For experimental therapy on intracranially-implanted NCH421k GBM, 32 tumor mice were randomized into 4 groups 3 days after the tumor implantation. 100 µl of the PBS or PBS containing FAM-$_D$[KLAKLAK]$_2$-NWs, FAM-PL1-NWs and FAM-PL1-$_D$[KLAKLAK]$_2$-NWs (5 mg/kg body weight of iron) were injected i.v. every other day for 10 total injections. Tumor size, body weight, survival, and behavior were recorded during and post-treatment. Kaplan–Meier survival and body weight curves were calculated using GraphPad Prism 6 and P values $<$ 0.05 were considered significant.

2.15. Statistical analysis

Prism 6 software was used to perform statistical analyses. The results are presented as mean with error bars indicating ± SEM. For comparison of 2 groups, we used unpaired *t*-test or ANOVA test ($p < 0.05$ was considered significant). P-values were considered as follows: *$p \leq 0.05$, **$p \leq 0.01$, ***$p \leq 0.001$ and p****≤ 0.0001. Details of analysis are shown in Table S3.

For animal study, the sample size was estimated on the basis of previous experiments yielding effect size 1,2 and 2.3 respectively [7] and unpublished data. Therefore, we conservatively assume effect size of 1.5 for sample calculation. To have at least > 80% probability of detecting a difference in means between the control and peptide-conjugated nanoparticle group of 2.2 standard deviations, we assigned a

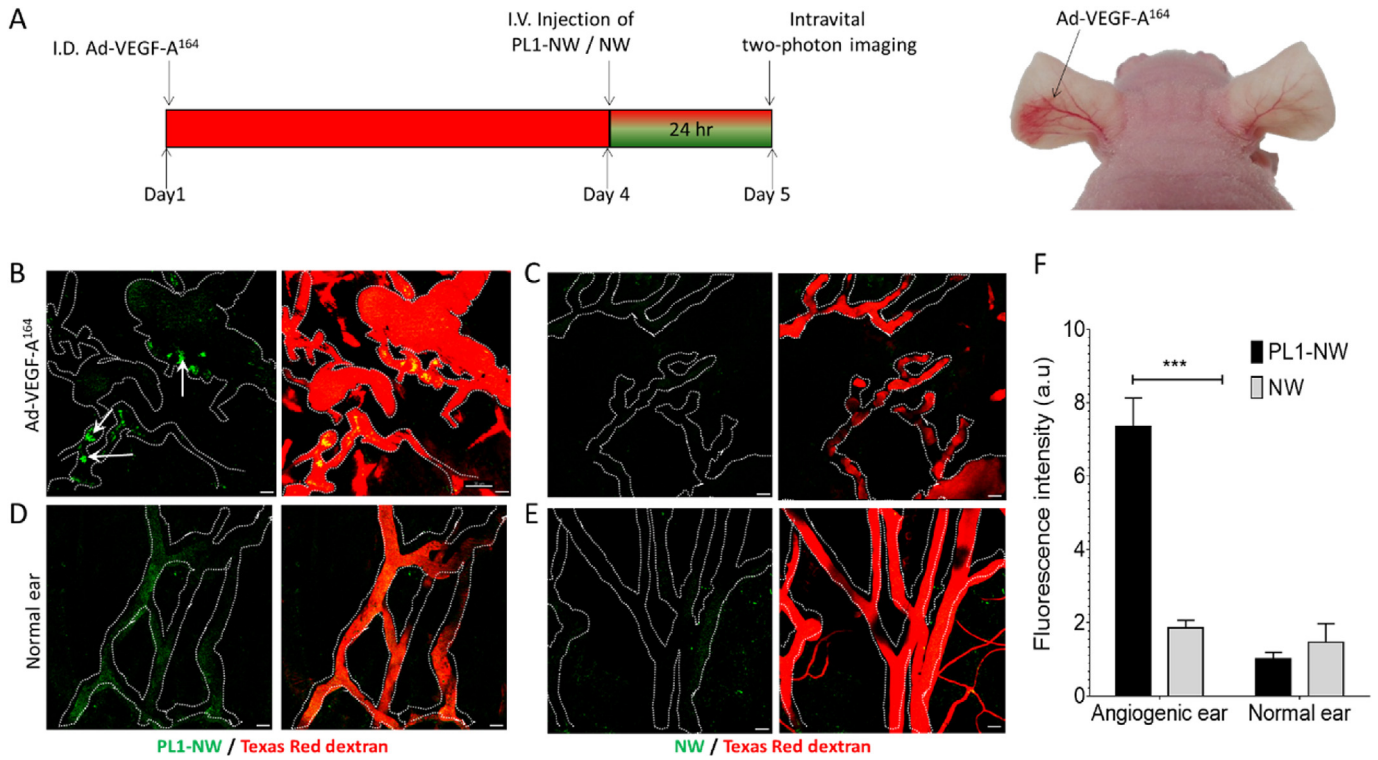

Fig. 4. PL1 NWs home to nonmalignant angiogenic vessels. (A) Left ear of nude athymic mice was intradermally injected with Ad-VEGF-A164; 4 days later, the angiogenic response was apparent, and the animal was injected with PL1-NWs for homing studies and multiphoton imaging after 24 h. (B) PL1-NWs accumulate in the angiogenic blood vessels. (C) Non-targeted NWs show no homing to the Ad-VEGF-A164 induced angiogenic site. (D, E) PL1-NWs and nontargeted NWs show no signal in the normal ear vessels. Green: PL1-NWs or NWs; red: blood vessels stained by Texas Red/Evans Blue, the dashed white lines delineate the vascular tree, arrows point to PL1-NWs in the angiogenic vessels. Scale bars: 20 μm. (F) Quantification of FAM signals in representative images (mean pixel intensity). Error bars: mean ± SEM (N = 3 mice per group), statistical analysis: p-value determined using two-tailed unpaired *t*-test; ***P < 0.001.

sample size of 8 mice in each treatment group. Sample size calculations were performed in PASS (NCSS 2008) or G Power [25] power analysis software using the Inequality Tests for Two Means procedure. NCH421k animals were blindly assigned to experimental or control groups. U87 animals were randomly assigned to experimental or control groups once tumor reached 100 mm^3. None of the animals were excluded from the analysis. No blinding was used during the experiment. Our experimental design ensures that minimal bias (or noise) is introduced, that could be mistaken as being treatment effects (by ensuring same sex, similar animal weight at start of experiment, same animal age, same type of stabling, several animals caged together).

3. Results

3.1. Identification of a bispecific TNC-C and FN-EDB binding peptide

For selection of bispecific peptides for FN-EDB and TNC-C, we employed cross-screening of X7 peptide libraries displayed on T7 phage on recombinant human FN-EDB and TNC-C fragments (Figs. S1 and S2). The first round of biopanning was performed on TNC-C immobilized on polystyrene multiwall plates, followed by several rounds of selection on hexahistidine-tagged FN-EDB coated onto magnetic Ni-NTA beads. By round 5, > 1000 fold enrichment in phage binding was seen (Fig. 1A). Whereas most of the 48 peptide phages individually tested from round 5 pool conferred phage binding to either target alone, a 27-amino acid (aa) peptide PPRRGLIKLKTSSNTKENSVVASLRP (PL5) possessed the desired dual binding ability (Fig. S3). The genome of the PL5 phage harbored a single nucleotide deletion in the peptide-encoding segment resulting in frameshift and conversion of 7-aa peptide displayed at the C-terminus of the phage major capsid protein to a 27-aa peptide (Fig. 1B). We created a panel of shorter derivatives of the PL5 peptide and found that 12-aa peptide, which we designated PL1 (PPRRGLIKLKTS), retained the ability to bind to both FN-EDB and TNC-C when displayed on phage particles (Fig. 1C) and as a synthetic FAM-labeled peptide (Fig. 1D). The binding was specific: PL1 phage did not interact with a recombinant control protein NRP-1, and the phage binding was inhibited by function-blocking polyclonal antibodies against FN-EDB and TNC-C (Fig. 1C). Alanine scanning mutagenesis showed that the PL1 peptide interacts with FN-EDB and TNC-C using an overlapping binding site, with L6 and T11 playing a critical role in both interactions (Fig. S4).

3.2. PL1-functionalized iron oxide nanoparticles home to tumor lesions

To explore the utility of PL1 peptide as a systemic tumor-targeting probe, we first studied the effect of PL1 coating on biodistribution of dextran-coated PEGylated paramagnetic iron oxide nanoworms (NW) – a model nanoscale agent used for systemic affinity targeting as a drug carrier and an MRI contrast agent [23]. PL1-NWs (Fig. S5) were audited for homing upon systemic administration in mice bearing orthotopic GBM (NCH421K, WT-GBM), s.c. GBM (U87MG), and prostate carcinoma (PC3) xenografts. Compared to non-targeted control NWs, PL1 functionalization increased accumulation of the NWs in the tumor perivascular matrix in all models tested (Fig. 2, Fig. S6). Compared to non-targeted NWs, the increase in PL1-NW accumulation after 5 h circulation was 8.8-fold in NCH421K, 5-fold in U87MG, 3.3-fold in WT, and 4.7-fold in PC3 tumors, whereas in the control organs (the liver, kidney, spleen, and lung) the signal for PL1-functionalized and non-targeted NWs was similar (Figs. S5 and S6). The fluorescence microscopy data were confirmed by Prussian blue histochemical staining for iron and light microscopy (Fig. S8). Preferential accumulation of PL1-NWs in NCH421k tumor tissue was also seen at 24 h time point (Fig.

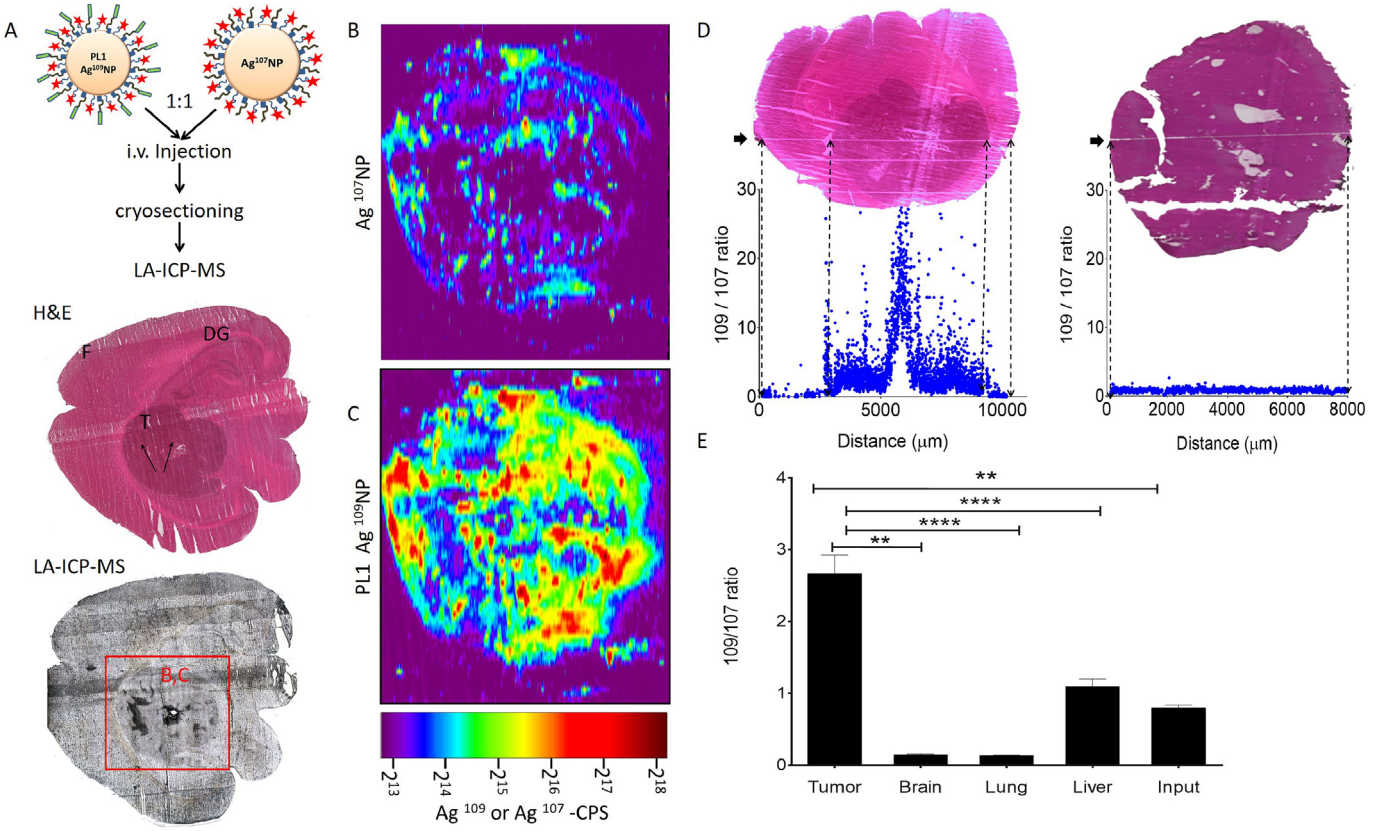

Fig. 5. Analysis of distribution of PL1-functionalized and control AgNPs by laser ablation inductively coupled plasma mass spectrometry (LA-ICP-MS). (A) Schematic illustration of the experimental procedure. Mice bearing orthotopic U87MG xenografts were injected i.v. with an equimolar mixture of targeted PL1-Ag109NPs and control Ag107NPs. After 5 h circulation and perfusion, organs were snap-frozen and sectioned at 30 μm for LA-ICP-MS. GBM is apparent in the H&E stained cryosections as an area of elevated cellular density. The region subjected to LA-ICP-MS analysis is outlined by a red box. (B–C) Distribution of control Ag107NPs (upper panel) and targeted PL1-Ag109NPs (lower panel) in the tumor and surrounding brain parenchyma. The color scale corresponds to isotope counts per second; the pixel size is 6.5 × 65 μm. Representative images of 3 independent experiments are shown. (D) Laser ablation line scans for Ag109/Ag107 profile using 40 μm spot diameter. The ablation path is indicated by an arrow in H&E-stained glioma brain (left) and control (liver) tissue (right). The blue-dot graphs show the Ag109/107 ratio on the laser ablation path across the tissue. (E) PL1-Ag109NP tissue distribution based on analysis of Ag109/107 ratios from line scans. PL1-AgNP concentration in glioma is 2.6 to 30-fold higher than in the control tissues. Data are representative of 3 independent animals. P-value was determined by one-way ANOVA Bonferroni's multiple comparisons test comparison with brain, lung and liver. Error bars: mean ± SD (n = 3 mice per group, each 5 data points per organ), **$p < 0.01$; ****$p < 0.0001$. Scale bars: 200 μm.

S6).

We next studied the relationship between the tumor homing pattern of the PL1-IONWs and the distribution of the FN-EDB and TNC-C immunoreactivities. Cryosections of U87MG and NCH421K tumors from PL1-NW-injected mice were stained with FN-EDB-specific (ScFV L19) and TNC-C-specific (ScFV G11) single-chain antibodies. Compared to normal organs, FN-EDB and TNC-C were upregulated in tumors (Fig. S9) and PL1-NW signal in tumor tissue showed extensive overlap with FN-EDB and TNC-C immunoreactivities (Fig. S10). Coadministration of PL1-NWs with blocking rabbit polyclonal antibodies against either FN-EDB or TNC-C resulted in a significant decrease in tumor homing and a cocktail of both FN-EDB and TNC-C antibodies almost completely inhibited the tumor accumulation of PL1-NWs (Fig. 2D). These results show that PL1-NWs home to tumor tissue in FN-EDB and TNC-C-dependent manner.

The elongated shape of NWs not only contributes to their ability to attach to target cells but also enhances magnetic relaxivity in MRI [23]. MRI was performed on NCH421K GBM mice pre-injection, 5 h after administration of systemic NWs and after terminal imaging. As shown in Fig. 3, T2-weighted and T2* images of tumors from mice injected with PL1-NWs tumors displayed a hypointense signal (Fig. 3). In contrast, in animals injected with nontargeted NWs, no changes in signal intensity within the tumors were observed under the same imaging conditions. In PL1-NW-injected mice, T2* relaxation time within the tumor decreased by 27–36% (from about 23 ± 2 ms to 17 ± 1 ms and 14 ± 4 ms). In mice injected with nontargeted NWs, relaxation time remained the same (21 ± 5 ms vs 22 ± 3 and 20 ± 6). Post-MRI confocal fluorescent imaging confirmed selective accumulation of PL1-NW in the GBMs (Fig. 3C). NCH421k is a clinically relevant stem cell-like GBM of intermediate phenotype and staining of tumor sections with anti-human stem and progenitor cell marker nestin antibodies was used to highlight the cancer stem cell-like cells (Fig. 3C). PL1-NWs were detected throughout the GBM lesions, including in the areas rich in nestin-positive cells. These results suggest potential applications for PL1-guided contrast agents as tumor-detecting and imaging agents.

FN-EDB and TNC-C are upregulated in angiogenic blood vessels during development and disease. To study the contribution of the angiogenesis-associated component to the homing of PL1, we next studied the biodistribution of PL1-NWs in mice having a locally-induced angiogenic response. Ears of nude mice were intradermally injected with an adenoviral vector driving the expression of VEGF-A164 (Fig. 4A). Four days after the injection of the adenovirus when both FN-EDB and TNC-C antigens were upregulated in angiogenic sites (Fig. S11), the animals were injected with Texas Red/Evans Blue to visualize patent blood vessels, followed by injection of PL1-NWs. *In vivo* multiphoton analysis showed a > 3-fold increase in accumulation of PL1-NWs

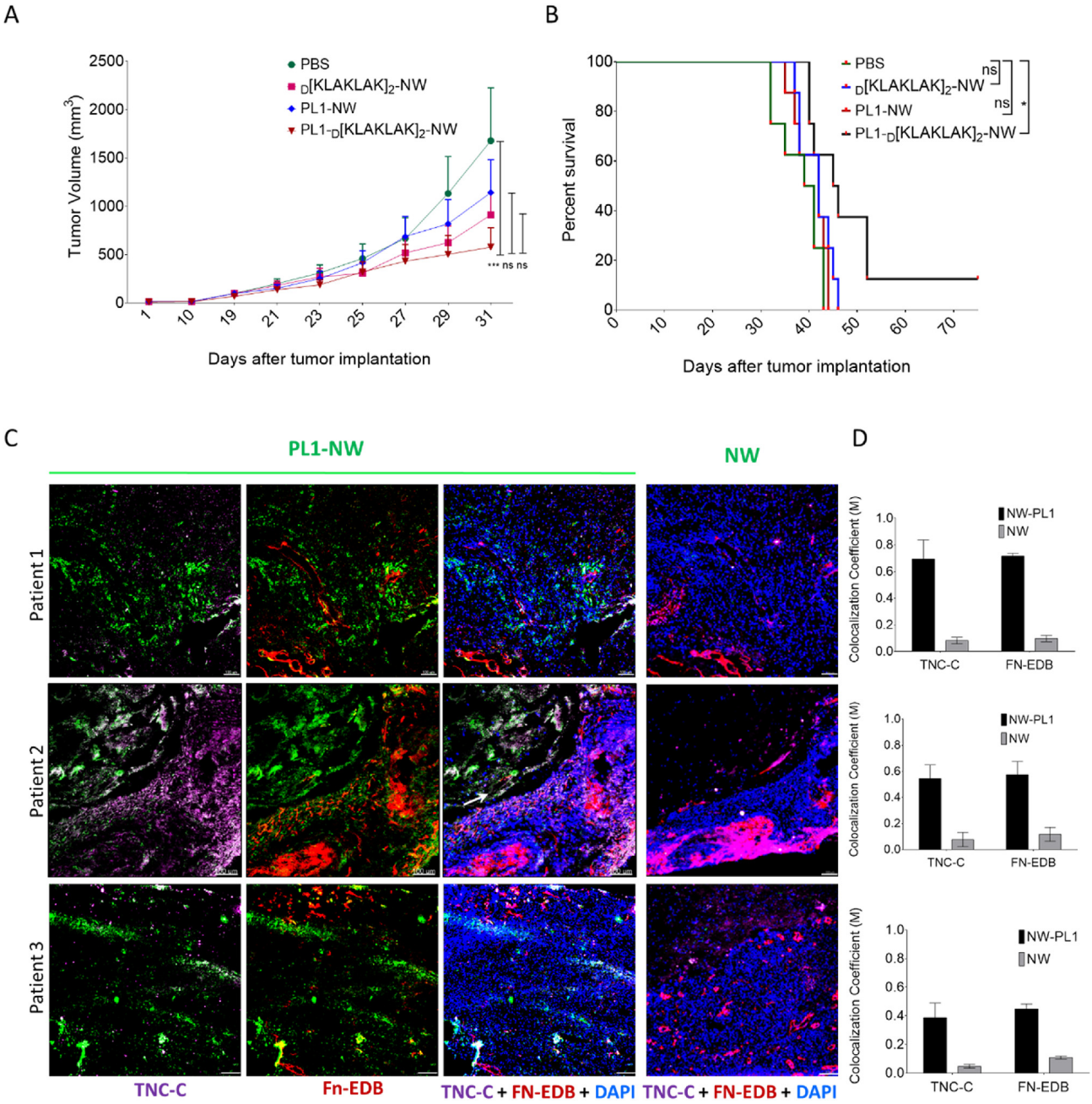

Fig. 6. Antitumor activity of PL1-targeted nanoworms on U87MG and NCH421K glioma models and PL1-NW overlay assay on clinical glioblastomas. Mice bearing subcutaneous U87MG and orthotopic NCH421K xenografts were i.v. injected with PBS, or different NWs formulations (D[KLAKLAK] 2-NWs, PL1-NWs or PL1-D [KLAKLAK] 2-NWs; all at 5 mg iron/kg). The injections were performed every other day for a total of 10 injections (n = 8 mice/group). (A) Dynamics of tumor volume in response to treatment with different NWs formulations. Statistical analyses were performed with two-way ANOVA Bonferroni's multiple comparisons test and log-rank test (n = 8 mice/group), error bars: mean ± SEM; ns - $P > 0.05$; *** - $p < 0.0001$; (B) Kaplan-Meier survival analysis. Mice bearing intracranial NCH421K tumors show statistically significant prolongation in survival when treated with PL1-D[KLAKLAK] 2-NWs compared to the control groups. (C) Frozen sections of individual patient tumors were incubated with PL1-NWs or nontargeted NWs, immunostained, and examined by confocal microscopy. PL1-NWs show binding to the tumor sections, and co-localize with EDB and TNC-C of all of the tested glioblastomas. Control non-targeted NWs exhibit no binding to the tumor sections. Tissues were stained for FAM (anti-FITC, green), EDB (ScFv L19, red), TNC-C (ScFv G11, magenta) and nuclei (DAPI, blue). Scale bar: 100 μm for all panels. (D) Colocalization analysis of PL1-NWs with EDB and TNC-C. Manders (M) correlation coefficient (0 - no colocalization; 1 - perfect colocalization) was calculated using Fiji ImageJ Coloc 2 plugin. Error bars, mean ± SEM.

(relative to nontargeted NWs) in the angiogenic vessels of adenovirus-injected ear but not in the contralateral normal ear (Fig. 4). Background labeling was seen in the blood vessels in the normal ear for both PL1 and control NWs (Fig. 4D–F, Fig. SM1-4). These results show that PL1 acts as an affinity ligand for angiogenic neovessels.

3.3. PL1-silver nanoparticles home to tumors

The structural and physicochemical properties of nanocarrier platform can have a dramatic effect on biodistribution and targetability with affinity ligands. To determine whether PL1 affinity targeting is compatible with precision delivery of nanocarriers other than NWs, we used silver nanoparticles (AgNP; Fig. S5)–a model nanoscale platform

that we have developed for biodistribution studies *in vitro* and *in vivo*. AgNPs plasmonically enhance the emission from surface fluorophores for ultrasensitive detection and can be isotopically barcoded for ultrasensitive detection by inductively-coupled plasma mass spectrometry (ICP) [26].

To quantify *in vivo* biodistribution of systemic PL1-AgNPs in tumor-bearing mice, we used ICP-MS to measure Ag. To overcome issues related to interanimal differences in dosing and physiological status of tumors, we injected tumor-bearing mice with a cocktail of isotopically-barcoded PL1-targeted and nontargeted AgNPs. Mice bearing orthotopic U87-MG GBM were i.v. injected with an equimolar mix of PL1-Ag^{109}NP and Ag^{107}NP (Fig. 5). After 5 h circulation tissues were collected and subjected to extract-based ICP-MS analysis and to line- and rasterized laser ablation mapping of the isotopic content by ICP-MS (LA-ICP-MS). ICP-MS analysis of tissue extracts demonstrated preferential tumor accumulation of PL1-Ag^{109}NPs (~190 μg/kg of Ag^{109}) over control Ag^{107}NPs (71 μg/kg of Ag^{107}), and similar levels of the two Ag isotopes in the control organs (Fig. S12). LA-ICP-MS mapping of intratumoral heterogeneity of Ag^{109}/Ag^{107} ratio showed heterogeneity, with some areas showing a Ag^{109}/Ag^{107} ratio of ~30 and above. Analysis of Ag^{109}/Ag^{107} ratio with LA-ICP-MS showed that PL1 functionalization increased AgNP homing to the GBMs on average ~2.7 fold (Fig. 5B–E). The homing of the PL1-Ag^{109}NPs was tumor-specific, as the Ag^{109}/Ag^{107} ratio in control organs was close to the input 1:1 ratio (liver), or lower (in the lung and normal brain).

3.4. PL1-targeted proapoptotic nanoparticles have anti-GBM activity

To determine the effect of the PL1 functionalization on therapeutic efficacy of anticancer nanoparticles, we used NWs coated with $_D$[KLAKLAK]$_2$ peptide as a model nanodrug. Chimeric $_D$[KLAKLAK]$_2$ -PL1 was covalently linked to the NWs through a 5K-polyethylene glycol (PEG) linker. In the first treatment study, we used s.c. U87MG tumors that express abundant FN-EDB and TNC-C and display an angiogenic well-perfused vasculature [27]. We chose to use subcutaneous model as it allowed us to monitor tumor size, rather than using survival, as the endpoint. Mice bearing s.c. U87MG tumors were treated with systemic injections every other day for 20 days. All mice from the PBS-treated group reached 2 cm^3 tumor volume allowed by animal ethics committee within 37 days after tumor induction and were sacrificed (Fig. 6A, Figs. S13–14). Tumor growth was significantly inhibited in the PL1- $_D$[KLAKLAK]$_2$-NW-treated group (Fig. 6A), whereas only a slight reduction in tumor growth was seen in animals treated with PL1-NWs, or $_D$[KLAKLAK]$_2$-NWs.

Next, we evaluated the anti-GBM efficacy of PL1-$_D$[KLAKLAK]$_2$-NWs in mice bearing human NCH421k orthotopic xenograft that displays a combination of angiogenic and infiltrative features. The treatment was initiated 3 days after tumor implantation. The median survival of NCH421k mice treated with PL1-D[KLAKLAK]2-NWs was significantly longer than of control mice treated with PBS, FAM-D[KLAKLAK]2-NWs, or PL1-NWs (Fig. 6B). Moreover, one mouse in the NCH421k group that received FAM-PL1- $_D$[KLAKLAK]$_2$-NWs survived 150 days without any clinical signs, suggesting a cure. There were no overt systemic toxicities as evidenced by stable body weight and normal histological appearance of organs from the treated animals (Fig. S13). Staining of tumor sections at the end of the treatment showed a significant decrease in the number of tumor CD31-positive blood vessels in the FAM-PL1-$_D$[KLAKLAK]$_2$-NW group compared with the control groups, whereas there was no difference between the treatment groups in tumor Ki67-positive cells, caspase-3-positive cells, CD11b, and CD68 macrophages or LYVE-1-positive lymphatic vessels (Fig. S14).

Finally, we studied the binding of PL1-NWs to clinical GBM samples. Cryosections of resected GBM were overlaid with FAM-PL1-NWs or FAM-labeled control NWs, washed and subjected to confocal imaging. PL1-NWs showed binding to all human GBM samples tested, with binding primarily at perivascular structures as well as deep in the tumor parenchyma (Fig. 6C–D). Overlaid PL1-NWs colocalized with tumor FN-EDB and TNC-C that are highly overexpressed in clinical GBM samples [28,29]. In contrast, control NWs showed only background fluorescence.

4. Discussion

Dual targeting with affinity ligands is a way of dealing with two critical issues of affinity targeting, that the number of molecules of any tumor-associated marker is limited and that there is considerable inter- and intratumoral heterogeneity in the expression of such markers [30,31]. Using two different tumor homing peptide modules in tandem can improve biodistribution of payloads within malignant tissues, but requires long, potentially immunogenic peptides [32]. Here we describe identification and preclinical development of a bispecific short peptide that contains overlapping binding sites for two clinically relevant ECM proteins, FN-EBD and TNC-C. Targeting with PL1 peptide increases homing of model nanoparticles in the FN-EDB and TNC-C positive areas in tumors and in angiogenic sites induced by overexpression of VEGF1 – a known inducer of FN-EDB expression [33,34]. In tumor tissue, FN-EDB and TNC-C have non-overlapping expression domains and targeting both receptors increases the likelyhood of PL1-receptor interaction and enthalpic gain for target-selective NP adsorption [35].

Systemically given PL1-functionalized nanoparticles home to tumors through participation of both receptor proteins. That this is the case, is evidenced by the fact that *in vivo* blockade of either receptor by a neutralizing antibody substantially decreases in FAM-PL1-NW accumulation in terms of both fluorescence intensity and area positive for the presence of the nanoparticles. Thus, dual targeting does increase the efficacy of the tumor targeting.

Low quantity and poor availability of receptors for affinity targeting have been recognized as major bottlenecks in the development of precision drugs. Tumor-associated ECM is higher capacity target for affinity delivery than membrane-bound receptors. For example, average molar representation of TNC subunits in tumor proteome is more than 2 orders of magnitude higher than the threshold level of HER2 considered positive and suitable for Herceptin-based therapies [36,37] ECM-targeted affinity therapeutics are not subject to lysosomal drug sequestration and inactivation upon endocytosis and act across tumor-resident cell populations including cells unaffected by therapeutic strategies aimed at the bulk of the tumor cells such as tumor stem cells, tumor fibroblasts (CAFs) and macrophages (TAMs) [38].

FN-EBD and TNC are abundant components of the tumor ECM and predictive of adverse outcome. Over the years, several monospecific targeting ligands have been developed for both FN-EDB [such as FN-EDB-ScFV L19 [39]] and TNC [e.g. TNC-C-ScFV G11 [14], TNC aptamer [40], and TNC-binding FHK peptide [41]]. Importantly, ECM-binding affinity ligands are compatible with targeting of intracellularly acting anticancer drugs: for example, ECM-binding antibody drug conjugates are able to efficiently release their drug payloads in the extracellular environment to exert a potent therapeutic activity [20,38]. We observed that treatment with systemic PL1- $_D$[KLAKLAK]$_2$-NWs significantly reduced tumor volume and increased the lifespan of tumor mice. To exert its apoptotic activity $_D$[KLAKLAK]$_2$ peptide must be primarily taken up in the cells and translocate to the mitochondria [42,43]. $_D$[KLAKLAK]$_2$, which is an amphiphilic peptide, is known to act as an internalizing agent, and $_D$[KLAKLAK]$_2$-NPs have been reported to be internalized into cells after having been brought to tumor tissue by a non-internalizing peptide [42]. Likewise, PL1- $_D$[KLAKLAK]$_2$-NWs introduced into tumor microenvironment are likely taken up in the cells in $_D$[KLAKLAK]$_2$-dependent manner. Short peptidic ligands tend to binds to conserved functionally important binding pockets on target molecules [5]. Both FN-EDB and TNC-C are involved in regulating endothelial cell behavior and plasticity during tumor angiogenesis. Our ongoing studies will elucidate PL1 binding site(s) on FN-EDB and TNC-C and establish whether engagement of PL1 peptide with its targets

alone may have an effect on tumor growth.

We used AgNPs to validate PL1 as a systemic, tumor-selective affinity ligand for nanoscale payloads because these NPs offer significant advantages regarding detection in tissues; they can be isotopically barcoded for ultrasensitive internally controlled detection and spatial mapping using LA-ICP-MS [44]. Tumor accumulation of PL1, and PL1-NPs in particular, may be limited by the accessibility of extravascular TNC-C and FN-EDB for blood-borne probes, which is likely to require leaky tumor blood vessels. Co-administration with tumor penetrating iRGD peptide has been shown to robustly increase the access of blood-borne probes for tumor HER2 (~6 fold) and αvβ3 integrin (~4 fold) [21]. It will be of great interest to explore if co-administered iRGD is also able to boost tumor accumulation of PL1-targeted payloads. Another aspect that must be systematically addressed is the selection of the type of drug and carrier best suited for PL1 targeting. Further studies are required to determine the effect of PL1 conjugation on the efficacy and toxicity profiles of conventional chemotherapeutics designed to be released in the extracellular space (e.g. through proteolytic cleavage or by reduction of disulfide bonds) [45,46] and on extracellularly-acting cytokines such as IL-2 and TNF-α [47,48]. Finally, the expression of both of the ECM targets of PL1 correlates with the cancer prognosis and therapeutic response profiles, suggesting that PL1 guided molecular imaging probes may have diagnostic and prognostic applications.

In summary, bispecific PL1 peptide allows specific targeting of solid tumors positive for expression of FN-EDB and/or TNC-C. As FN-EDB domain is fully and TNC-C domain is 96% conserved between mice and humans, it is possible to envision clinical development for PL1-based approaches for precision cancer drug delivery and application of PL1-guided imaging agents as companion diagnostics to stratify patients for therapeutic targeting FN-EDB and TNC-C-positive tumors and to monitor the efficacy of anticancer interventions.

Significance

Simultaneous affinity targeting of two or more markers in the tumor microenvironment may overcome the spatiotemporal heterogeneity in expression of target molecules and alleviate issues related to the limited number of available receptors for targeting ligands. We describe development of a simple 12 amino acid homing peptide for dual targeting of fibronectin and tenascin isoforms in the tumor extracellular matrix (ECM). FN-EDB and TNC-C domains targeted by the peptide are fully conserved between mouse and human and are already developed as targets of monospecific single chain antibodies. Features of PL1 peptide – dual targeting of abundant tumor-associated ECM components, specificity in binding to clinically relevant targets, small size, and human reactivity – warrant follow-up preclinical and clinical development.

Author contributions

PL – coordinated the study, performed the experiments, drafted the manuscript. AT – prepared and characterized the NPs. MH – helped in Ad-VEGF164 induced angiogenesis model and performed intravital imaging. HH –performed NW conjugation to targeting ligands. PP – carried out LA-ICP-MS experiments and analyzed the data. TA – provided access to clinical samples and data. TR – provided access to clinical samples and data. VRK –synthesized FAM-D[KLAKLAK]2, PL1, and PL1- D[KLAKLAK]2 peptides. RB – GBM modeling, data interpretation. TT – conception and supervising the study, writing the manuscript.

Conflicts of interest

The data that supports the findings of this study are available from the corresponding author upon request.

No competing interests.

Funding

This work was supported by the European Union through the European Regional Development Fund (Project No. 2014-2020.4.01.15-0012), by EMBO Installation Grant #2344, European Research Council grants GLIOMA DDS and GlioGuide from European Regional Development Fund and Wellcome Trust International Fellowship WT095077MA (TT), Cancer Center Support grant CA30199 from the US National Cancer Institute to the Sanford Burnham Prebys Medical Discovery Institute and grants from The Norwegian Cancer Society and the Norwegian Research Council.

Acknowledgments

We are grateful to Erkki Ruoslahti for critical reading and comments on the manuscript and Pille Säälik for help with setting up glioma models. We thank Harold F Dvorak for kind gift of Ad-VEGF-A164, Gabriele Bergers for WT GBM and VEGF KO GBM cells, Erkki Juronen for help with ÄKTA Protein Purification System, Indrek Heinla for help with MRI, Olivier Keunen for critical comments on MRI data, and Rein Laiverik for help with the characterization of the NWs.

Appendix A. Supplementary data

Supplementary data to this article can be found online at https://doi.org/10.1016/j.biomaterials.2019.119373.

References

[1] P.J. Kennedy, C. Oliveira, P.L. Granja, B. Sarmento, Antibodies and associates: partners in targeted drug delivery, Pharmacol. Ther. (2017), https://doi.org/10.1016/j.pharmthera.2017.03.004.
[2] E. Ruoslahti, Tumor penetrating peptides for improved drug delivery, Adv. Drug Deliv. Rev. (2016), https://doi.org/10.1016/j.addr.2016.03.008.
[3] J.M. Lambert, C.Q. Morris, Antibody–drug conjugates (ADCs) for personalized treatment of solid tumors: a review, Adv. Ther. (2017) 1–21, https://doi.org/10.1007/s12325-017-0519-6.
[4] P.J. Carter, G.A. Lazar, Next generation antibody drugs: pursuit of the "high-hanging fruit, Nat. Rev. Drug Discov. 17 (2018) 197–223, https://doi.org/10.1038/nrd.2017.227.
[5] T. Teesalu, K.N. Sugahara, E. Ruoslahti, Mapping of vascular ZIP codes by phage display, Methods Enzymol. 503 (2012) 35–56, https://doi.org/10.1016/B978-0-12-396962-0.00002-1.
[6] A.-M.A. Willmore, L. Simón-Gracia, K. Toome, P. Paiste, V.R. Kotamraju, T. Mölder, K.N. Sugahara, E. Ruoslahti, G.B. Braun, T. Teesalu, Targeted silver nanoparticles for ratiometric cell phenotyping, Nanoscale 8 (2016) 9096–9101, https://doi.org/10.1039/C5NR07928D.
[7] K.N. Sugahara, T. Teesalu, P.P. Karmali, V.R. Kotamraju, L. Agemy, O.M. Girard, D. Hanahan, R.F. Mattrey, E. Ruoslahti, Tissue-penetrating delivery of compounds and nanoparticles into tumors, Cancer Cell 16 (2009) 510–520, https://doi.org/10.1016/j.ccr.2009.10.013.
[8] L. Paasonen, S. Sharma, G.B. Braun, V.R. Kotamraju, T.D.Y. Chung, Z.G. She, K.N. Sugahara, M. Yliperttula, B. Wu, M. Pellecchia, E. Ruoslahti, T. Teesalu, New p32/gC1qR ligands for targeted tumor drug delivery, Chembiochem 17 (2016) 570–575, https://doi.org/10.1002/cbic.201500564.
[9] S. Christian, J. Pilch, M.E. Akerman, K. Porkka, P. Laakkonen, E. Ruoslahti, Nucleolin expressed at the cell surface is a marker of endothelial cells in angiogenic blood vessels, J. Cell Biol. 163 (2003) 871–878, https://doi.org/10.1083/jcb.200304132.
[10] L. Xing, Y. Xu, K. Sun, H. Wang, F. Zhang, Z. Zhou, J. Zhang, F. Zhang, B. Caliskan, Z. Qiu, M. Wang, Identification of a peptide for folate receptor alpha by phage display and its tumor targeting activity in ovary cancer xenograft, Sci. Rep. 8 (2018) 8426, https://doi.org/10.1038/s41598-018-26683-z.
[11] D. Simberg, T. Duza, J.H. Park, M. Essler, J. Pilch, L. Zhang, A.M. Derfus, M. Yang, R.M. Hoffman, S. Bhatia, M.J. Sailor, E. Ruoslahti, Biomimetic amplification of nanoparticle homing to tumors, Proc. Natl. Acad. Sci. U.S.A. 104 (2007) 932–936, https://doi.org/10.1073/pnas.0610298104.
[12] S. Mitra, S. Duggineni, M. Koolpe, X. Zhu, Z. Huang, E.B. Pasquale, Structure-activity relationship analysis of peptides targeting the EphA2 receptor, Biochemistry 49 (2010) 6687–6695, https://doi.org/10.1021/bi1006223.
[13] H. Järveläinen, Extracellular matrix molecules: potential targets in pharmacotherapy, Pharmacol. Rev. 61 (2009) 198–223, https://doi.org/10.1124/pr.109.001289.provided.
[14] M. Silacci, S.S. Brack, N. Späth, A. Buck, S. Hillinger, S. Arni, W. Weder, L. Zardi, D. Neri, Human monoclonal antibodies to domain C of tenascin-C selectively target solid tumors in vivo, Protein Eng. Des. Sel. 19 (2006) 471–478, https://doi.org/10.1093/protein/gzl033.

[15] B. Carnemolla, P. Castellani, M. Ponassi, L. Borsi, S. Urbini, G. Nicolo, A. Dorcaratto, G. Viale, G. Winter, D. Neri, L. Zardi, Identification of a glioblastoma-associated tenascin-C isoform by a high affinity recombinant antibody, Am. J. Pathol. 154 (1999) 1345–1352, https://doi.org/10.1016/S0002-9440(10)65388-6.
[16] J. Park, S. Kim, P.E. Saw, I.H. Lee, M.K. Yu, M. Kim, K. Lee, Y.C. Kim, Y.Y. Jeong, S. Jon, Fibronectin extra domain B-specific aptide conjugated nanoparticles for targeted cancer imaging, J. Control. Release 163 (2012) 111–118, https://doi.org/10.1016/j.jconrel.2012.08.029.
[17] H. Kumra, D.P. Reinhardt, Fibronectin-targeted drug delivery in cancer, Adv. Drug Deliv. Rev. 97 (2016) 101–110, https://doi.org/10.1016/j.addr.2015.11.014.
[18] C. Spenlé, F. Saupe, K. Midwood, H. Burckel, G. Noel, G. Orend, Tenascin-C, Exploitation and collateral damage in cancer management, Cell Adhes. Migrat. 9 (2015) 141–153, https://doi.org/10.1080/19336918.2014.1000074.
[19] G. Akabani, D.A. Reardon, R.E. Coleman, T.Z. Wong, S.D. Metzler, J.E. Bowsher, D.P. Barboriak, J.M. Provenzale, K.L. Greer, D. DeLong, H.S. Friedman, A.H. Friedman, X.-G. Zhao, C.N. Pegram, R.E. McLendon, D.D. Bigner, M.R. Zalutsky, Dosimetry and radiographic analysis of 131I-labeled anti-tenascin 81C6 murine monoclonal antibody in newly diagnosed patients with malignant gliomas: a phase II study, J. Nucl. Med. 46 (2005) 1042–1051 http://www.ncbi.nlm.nih.gov/pubmed/15937318 , Accessed date: 17 April 2017.
[20] A. Dal Corso, R. Gébleux, P. Murer, A. Soltermann, D. Neri, A non-internalizing antibody-drug conjugate based on an anthracycline payload displays potent therapeutic activity in vivo, J. Control. Release 264 (2017) 211–218, https://doi.org/10.1016/j.jconrel.2017.08.040.
[21] S. Hussain, M. Rodriguez-Fernandez, G.B. Braun, F.J. Doyle, E. Ruoslahti, Quantity and accessibility for specific targeting of receptors in tumours, Sci. Rep. 4 (2014) 5232, https://doi.org/10.1038/srep05232.
[22] T. Teesalu, K.N. Sugahara, V.R. Kotamraju, E. Ruoslahti, C-end rule peptides mediate neuropilin-1-dependent cell, vascular, and tissue penetration, Proc. Natl. Acad. Sci. U.S.A. 106 (2009) 16157–16162, https://doi.org/10.1073/pnas.0908201106.
[23] J.-H. Park, G. von Maltzahn, L. Zhang, M.P. Schwartz, E. Ruoslahti, S.N. Bhatia, M.J. Sailor, Magnetic iron oxide nanoworms for tumor targeting and imaging, Adv. Mater. 20 (2008) 1630–1635, https://doi.org/10.1002/adma.200800004.
[24] J.A. Nagy, S. Shih, W.H. Wong, A.M. Dvorak, H.F. Dvorak, Chapter 3. The adenoviral vector angiogenesis/lymphangiogenesis assay, Methods Enzymol. 444 (2008) 43–64, https://doi.org/10.1016/S0076-6879(08)02803-6.
[25] F. Faul, E. Erdfelder, A.G. Lang, A. Buchner, G*Power 3: a flexible statistical power analysis program for the social, behavioral, and biomedical sciences, Behav. Res. Methods (2007) 175–191, https://doi.org/10.3758/BF03193146.
[26] G.B. Braun, T. Friman, H.-B. Pang, A. Pallaoro, T. Hurtado de Mendoza, A.-M.A. Willmore, V.R. Kotamraju, A.P. Mann, Z.-G. She, K.N. Sugahara, N.O. Reich, T. Teesalu, E. Ruoslahti, Etchable plasmonic nanoparticle probes to image and quantify cellular internalization, Nat. Mater. 13 (2014) 904–911, https://doi.org/10.1038/nmat3982.
[27] M. Candolfi, J.F. Curtin, W.S. Nichols, A.K.M.G. Muhammad, G.D. King, G.E. Pluhar, E.A. McNiel, J.R. Ohlfest, A.B. Freese, P.F. Moore, J. Lerner, P.R. Lowenstein, M.G. Castro, Intracranial glioblastoma models in preclinical neuro-oncology: neuropathological characterization and tumor progression, J. Neuro Oncol. 85 (2007) 133–148, https://doi.org/10.1007/s11060-007-9400-9.
[28] M. Pedretti, C. Verpelli, J. Mårlind, G. Bertani, C. Sala, D. Neri, L. Bello, Combination of temozolomide with immunocytokine F16-IL2 for the treatment of glioblastoma, Br. J. Canc. 103 (2010) 827–836, https://doi.org/10.1038/sj.bjc.6605832.
[29] B. Carnemolla, P. Castellani, M. Ponassi, L. Borsi, S. Urbini, G. Nicolo, A. Dorcaratto, G. Viale, G. Winter, D. Neri, L. Zardi, Identification of a glioblastoma-associated Tenascin-C isoform by a high affinity recombinant antibody, Am. J. Pathol. 154 (1999) 1345–1352, https://doi.org/10.1016/S0002-9440(10)65388-6.
[30] N. Wang, R.K. Jain, T.T. Batchelor, New directions in anti-angiogenic therapy for glioblastoma, Neurotherapeutics (2017), https://doi.org/10.1007/s13311-016-0510-y.
[31] E.B. Ehlerding, L. Sun, X. Lan, D. Zeng, W. Cai, Dual-targeted molecular imaging of cancer, J. Nucl. Med. 117 (2018) 199877, https://doi.org/10.2967/jnumed.117.199877 jnumed.
[32] S. Süer, H. Baloğlu, Z. Güngör, H. Sönmez, E. Kökoğlu, The distribution of tissue fibronectin and sialic acid in human breast cancer, Cancer Biochem. Biophys. 16 (1998) 63–70 http://www.ncbi.nlm.nih.gov/pubmed/9923968 , Accessed date: 26 March 2019.
[33] Z.A. Khan, B.M. Chan, S. Uniyal, Y.P. Barbin, H. Farhangkhoee, S. Chen, S. Chakrabarti, EDB fibronectin and angiogenesis - a novel mechanistic pathway, Angiogenesis 8 (2005) 183–196, https://doi.org/10.1007/s10456-005-9017-6.
[34] E. Trachsel, M. Kaspar, F. Bootz, M. Detmar, D. Neri, A human mAb specific to oncofetal fibronectin selectively targets chronic skin inflammation in vivo, J. Investig. Dermatol. 127 (2007) 881–886, https://doi.org/10.1038/sj.jid.5700653.
[35] S. Wang, E.E. Dormidontova, Selectivity of ligand-receptor interactions between nanoparticle and cell surfaces, Phys. Rev. Lett. 109 (2012) 238102, https://doi.org/10.1103/PhysRevLett.109.238102.
[36] D.A. Olsen, T. Bechmann, B. Østergaard, P.A. Wamberg, E.H. Jakobsen, I. Brandslund, Increased concentrations of growth factors and activation of the EGFR system in breast cancer, Clin. Chem. Lab. Med. 50 (2012) 1809–1818, https://doi.org/10.1515/cclm-2011-0823.
[37] S. Riedl, M. Kadmon, A. Tandara, U. Hinz, P. Möller, C. Herfarth, A. Faissner, Mucosal tenascin C content in inflammatory and neoplastic diseases of the large bowel, Dis. Colon Rectum 41 (1998) 86–92, https://doi.org/10.1007/BF02236901.
[38] R. Raavé, T.H. van Kuppevelt, W.F. Daamen, Chemotherapeutic drug delivery by tumoral extracellular matrix targeting, J. Control. Release 274 (2018) 1–8, https://doi.org/10.1016/j.jconrel.2018.01.029.
[39] F. Nilsson, H. Kosmehl, L. Zardi, D. Neri, Targeted delivery of tissue factor to the ED-B domain of fibronectin, a marker of angiogenesis, mediates the infarction of solid tumors in mice, Cancer Res. 61 (2001) 711–716 http://www.ncbi.nlm.nih.gov/pubmed/11212273 , Accessed date: 21 September 2016.
[40] D. a Daniels, H. Chen, B.J. Hicke, K.M. Swiderek, L. Gold, A tenascin-C aptamer identified by tumor cell SELEX: systematic evolution of ligands by exponential enrichment, Proc. Natl. Acad. Sci. U.S.A. 100 (2003) 15416–15421, https://doi.org/10.1073/pnas.2136683100.
[41] M.Y. Kim, O.R. Kim, Y.S. Choi, H. Lee, K. Park, C.T. Lee, K.W. Kang, S. Jeong, Selection and characterization of tenascin C targeting peptide, Mol. Cells 33 (2012) 71–77, https://doi.org/10.1007/s10059-012-2214-4.
[42] L. Agemy, D. Friedmann-Morvinski, V.R. Kotamraju, L. Roth, K.N. Sugahara, O.M. Girard, R.F. Mattrey, I.M. Verma, E. Ruoslahti, Targeted nanoparticle enhanced proapoptotic peptide as potential therapy for glioblastoma, Proc. Natl. Acad. Sci. 108 (2011) 17450–17455, https://doi.org/10.1073/pnas.1114518108.
[43] H.M. Ellerby, W. Arap, L.M. Ellerby, R. Kain, R. Andrusiak, G.D. Rio, S. Krajewski, C.R. Lombardo, R. Rao, E. Ruoslahti, D.E. Bredesen, R. Pasqualini, Anticancer activity of targeted proapoptotic peptides, Nat. Med. 5 (1999) 1032–1038, https://doi.org/10.1038/12469.
[44] K. Toome, A.-M.A. Willmore, P. Paiste, A. Tobi, K.N. Sugahara, K. Kirsimäe, E. Ruoslahti, G.B. Braun, T. Teesalu, Ratiometric in vivo auditioning of targeted silver nanoparticles, Nanoscale 9 (2017) 10094–10100, https://doi.org/10.1039/c7nr04056c.
[45] X. Guo, Y. Cheng, X. Zhao, Y. Luo, J. Chen, W.-E. Yuan, Advances in redox-responsive drug delivery systems of tumor microenvironment, J. Nanobiotechnol. 16 (2018) 74, https://doi.org/10.1186/s12951-018-0398-2.
[46] E. Perrino, M. Steiner, N. Krall, G.J.L. Bernardes, F. Pretto, G. Casi, D. Neri, Curative properties of noninternalizing antibody-drug conjugates based on maytansinoids, Cancer Res. 74 (2014) 2569–2578, https://doi.org/10.1158/0008-5472.CAN-13-2990.
[47] A. Johansson, J. Hamzah, R. Ganss, License for destruction: tumor-specific cytokine targeting, Trends Mol. Med. 20 (2014) 16–24, https://doi.org/10.1016/j.molmed.2013.10.002.
[48] B. Carnemolla, L. Borsi, E. Balza, P. Castellani, R. Meazza, A. Berndt, S. Ferrini, H. Kosmehl, D. Neri, L. Zardi, Enhancement of the antitumor properties of interleukin-2 by its targeted delivery to the tumor blood vessel extracellular matrix, Blood 99 (2002) 1659–1665, https://doi.org/10.1182/blood.V99.5.1659.